INTERFACE

rsif.royalsocietypublishing.org

Research

Cite this article: Ghoshal A, Eck E, Gordon M, Morse DE. 2016 Wavelength-specific forward scattering of light by Bragg-reflective iridocytes in giant clams. *J. R. Soc. Interface* **13**: 20160285.
http://dx.doi.org/10.1098/rsif.2016.0285

Received: 10 April 2016
Accepted: 16 June 2016

Subject Category:
Life Sciences–Physics interface

Subject Areas:
biomaterials, biophysics, biomimetics

Keywords:
Tridacna, *Symbiodinium*, solar, photonic, refractive index, Mie

Author for correspondence:
Daniel E. Morse
e-mail: d_morse@lifesci.ucsb.edu

Electronic supplementary material is available at http://dx.doi.org/10.1098/rsif.2016.0285 or via http://rsif.royalsocietypublishing.org.

THE ROYAL SOCIETY PUBLISHING

Wavelength-specific forward scattering of light by Bragg-reflective iridocytes in giant clams

Amitabh Ghoshal[1], Elizabeth Eck[2], Michael Gordon[1,3] and Daniel E. Morse[1,2]

[1]Institute for Collaborative Biotechnologies, [2]Department of Molecular, Cellular and Developmental Biology, and [3]Department of Chemical Engineering, University of California, Santa Barbara, CA 93106-5100, USA

DEM, 0000-0002-0247-9110

A surprising recent discovery revealed that the brightly reflective cells ('iridocytes') in the epithelia of giant clams actually send the majority of incident photons 'forward' into the tissue. While the intracellular Bragg reflectors in these cells are responsible for their colourful back reflection, Mie scattering produces the forward scattering, thus illuminating a dense population of endosymbiotic, photosynthetic microalgae. We now present a detailed micro-spectrophotometric characterization of the Bragg stacks in the iridocytes in live tissue to obtain the refractive index of the high-index layers (1.39 to 1.58, average 1.44 ± 0.04), the thicknesses of the high- and low-index layers (50–150 nm), and the numbers of pairs of layers (2–11) that participate in the observed spectral reflection. Based on these measurements, we performed electromagnetic simulations to better understand the optical behaviour of the iridocytes. The results open a deeper understanding of the optical behaviour of these cells, with the counterintuitive discovery that specific combinations of iridocyte diameter and Bragg-lamellar spacing can produce back reflection of the same colour that is also scattered forward, in preference to other wavelengths that are scattered at higher angles. We find for all values of size and wavelength investigated that more than 90% of the incident energy is carried by the photons that are scattered in the forward direction; while this forward scattering from each iridocyte shows very narrow angular dispersion (*ca* $\pm 6^\circ$), the multiplicative scattering from a layer of *ca* 20 iridocytes broadens this dispersion to a cone of approximately $\pm 90^\circ$. This understanding of the complex biophotonic dynamics enhances our comprehension of the physiologically, ecologically and evolutionarily significant light environment inside the giant clam, which is diffuse and nearly white at small tissue depths and downwelling, relatively monochromatic, and can be the same colour as the back-reflected light at greater depths in the tissue. Originally thought to be unique, cells of similar structure and photonic activity are now recognized in other species, where they serve other functions. The behaviour of the iridocytes opens possible new considerations for conservation and management of the valuable giant clam resource and new avenues for biologically inspired photonic applications.

1. Introduction

Giant clams (family Tridacnidae) are native to the coral reefs of the tropical Pacific and Indian Oceans [1]. In spite of living in nutrient-poor waters [2–4], the clams can grow up to 1.4 m long [5]. Such large sizes are attainable largely due to the dense cultures of endosymbiotic microalgae of the genus *Symbiodinium* that clams maintain within their tissues [6–11]. Like the reef-building corals that also host members of this algal genus, the giant clams depend on the photosynthesis of these symbionts to produce vital nutrients that support their growth in the oligotrophic and plankton-poor waters of the tropical reef, and to modulate the carbonate equilibria controlling the rapid calcification of their shells [12–16].

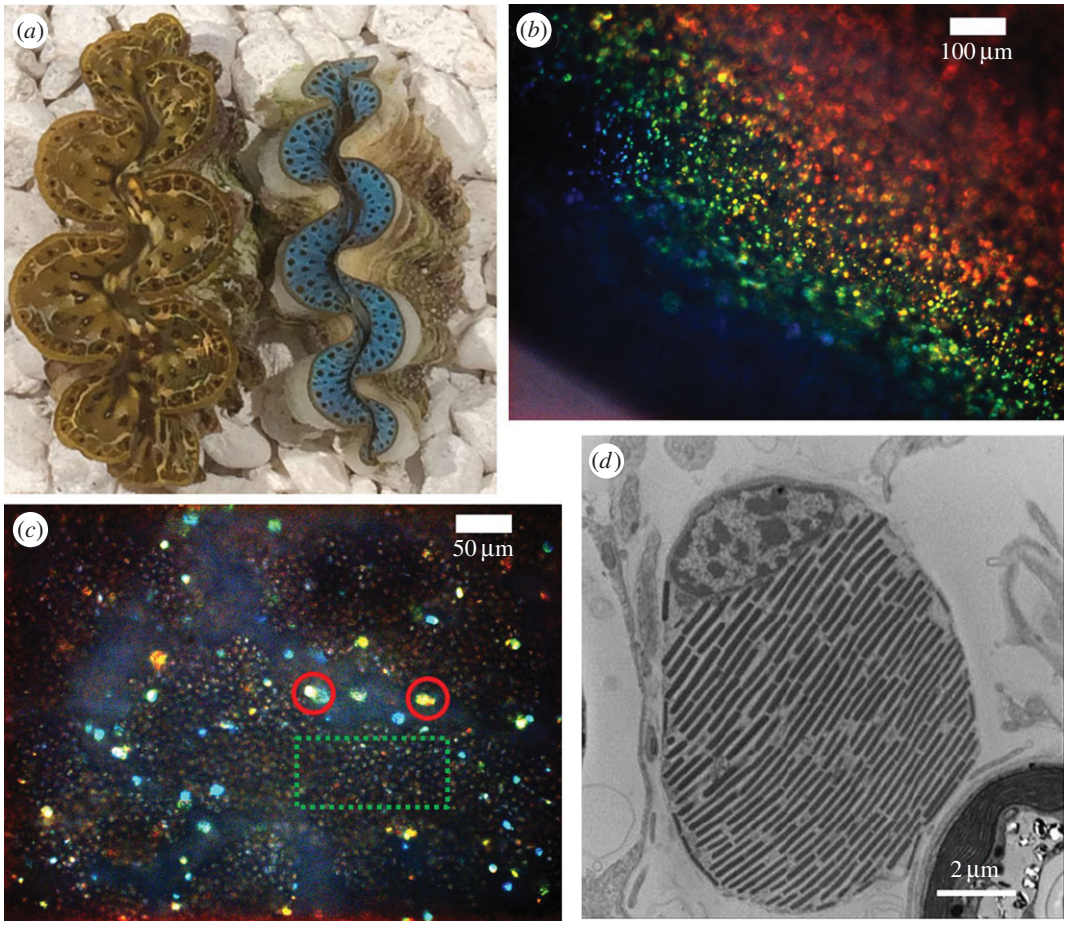

Figure 1. Macro- and microscopic views of *Tridacna maxima* and *T. derasa*. (*a*) Top view of two *T. maxima* approximately 4–5 cm in length. (*b*) Magnified view (dark-field) of the mantle of *T. derasa*; individual bright spots are iridocytes. Outer edge of the mantle is at lower left. (*c*) Higher magnification (dark-field) image of the specimen shown in (*b*). The bright coloured spots, two of which are circled in solid red, are iridocytes; the small dark spots, a sample region of which is marked with a green dashed square, are symbiotic microalgae. (*d*) Transmission electron micrograph of a *T. derasa* iridocyte in cross section; fixation with glutaraldehyde and staining with osmium tetroxide, from [28] (reproduced with permission). Darkly stained, brick-like lamellae correspond to electron-opaque, protein-rich, high-index layers separated by low refractive index spaces of the Bragg reflector.

In addition to their endosymbiotic algae, giant clams are distinguished by the brilliantly iridescent blue, green and gold colours they display. This colouration is due to light reflected from unique iridescent cells (called 'iridocytes') in their epithelia, similar to the iridocytes of other molluscs such as squids and cuttlefish [17–21]. As in these other molluscs, the giant clam iridocytes contain intracellular reflective structures consisting of periodic, alternating layers of high and low refractive index that form Bragg lamellae [12,22–24]. The iridocytes in giant clams are unique, however, in being predominantly spherical and smaller (approx. 5–15 µm) than the large (*ca* 100 µm) flat iridocytes in squids and cuttlefishes [19–21,25,26]. The optical characteristics and functional significance of the giant clam iridocytes have been the subject of many attempts at elucidation, with suggestions for their activities ranging from sunscreens [27] to enhancers of algal photosynthesis by forward light scattering [28]. As the giant clams are able to thrive in nutrient-poor waters as a result of the photosynthetic activity of their *Symbiodinium*, the symbiotic complex can be treated as a model system for investigations of highly efficient light harvesting and solar energy conversion.

Here, we present an *in vivo* optical characterization of live iridocytes in the mantle of three species of giant clam, in conjunction with characterization of the physical properties of the Bragg-lamellar structures. We find that the average refractive index of the high-index region of the Bragg structures is 1.44 ± 0.04, while spanning the range 1.39–1.58. Typically, 2–11 pairs of high and low refractive index lamellae generate the observed reflections, and the thicknesses of these layers vary from 50 to 150 nm, although the high-index layers tend to be thicker by approximately 20 nm. Based on these optical measurements and fitted, computational correlations with the physical structures of the Bragg reflectors, we present electromagnetic finite difference time domain (FDTD) simulations of iridocytes that reveal several unanticipated optical behaviours. The most counterintuitive behaviour observed is that at wavelengths at which the iridocyte reflects light (given the right cell size) the iridocyte also scatters *more light forward than a simple spherical particle* of the same diameter and average refractive index. The results we report support the suggested role of forward scattering, introduce new biological considerations and open possibilities for application to optical, solar- and other photo-transductive devices.

2. Material and methods

2.1. Micro-spectrophotometry

Two specimens of the giant clam, *Tridacna maxima*, are shown exhibiting typical behaviour during daylight hours, with the brightly reflective mantle deployed as a solar collector for algal photosynthesis overlapping the shell (figure 1*a*). Images of the

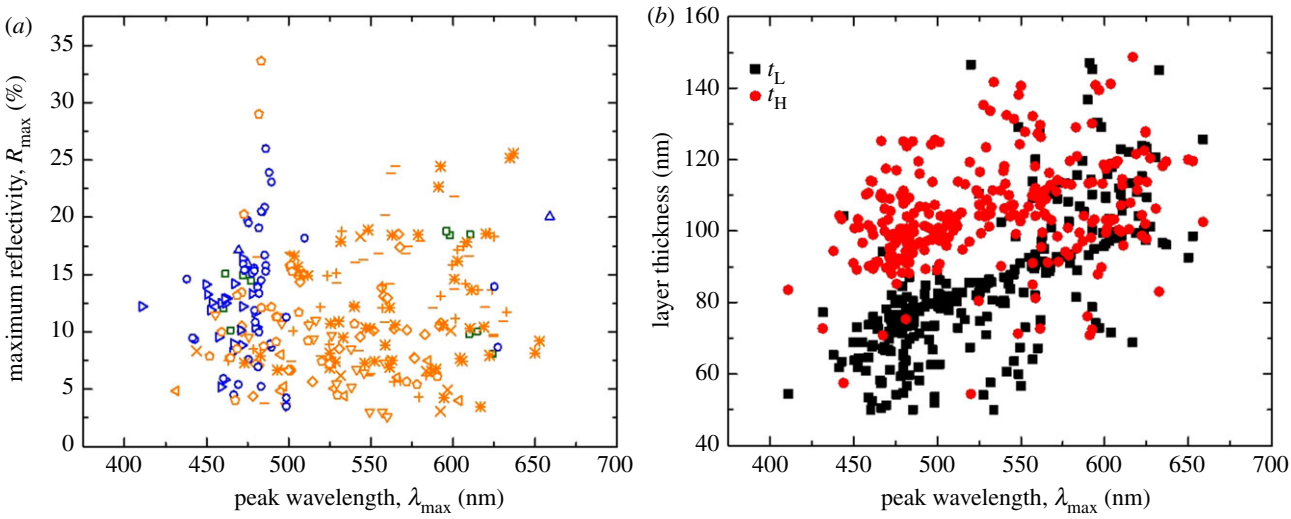

Figure 2. Optical and structural parameters of iridocytes in *Tridacna crocea*, *T. maxima*, and *T. derasa*. (*a*) Peak reflectivity, R_{max}, versus peak wavelength, λ_{max}, measured for individual iridocytes from *T. derasa* (orange; seven specimens as indicated), *T. crocea* (blue; three specimens) and *T. maxima* (green; one specimen); iridocytes from different individual specimens are indicated with different symbols. (*b*) Lamellar thicknesses obtained from fitting, as a function of measured peak wavelength; t_H = thickness of high refractive index layer (red circles); t_L = thickness of the low-index layer (black squares).

excised mantle tissue of a congenric *Tridacna derasa*, with the outer surface of the mantle towards the microscope objective, are shown in figure 1*b*,*c*. Figure 1*b* shows a population of iridocytes ranging from blue to red located at various depths in the mantle tissue. Figure 1*c* shows the mantle tissue at a higher magnification, where individual iridocytes (circled in red) and algal cells (marked by the dashed green square) are clearly resolved. For reference, figure 1*d* (reproduced from [28]) shows the intracellular Bragg lamellae responsible for the spectral reflection of iridocytes as previously discussed [22–24].

Reflection spectra were collected from individual and well-isolated iridocytes, from areas smaller than 1 µm in diameter in bright-field mode, using an imaging spectrometer (Horiba JobinYvon iHR320, Horiba Group, Kyoto, Japan) with a Synapse thermoelectrically cooled charge coupled device connected to a Zeiss AxioObserver D1M inverted microscope (Carl Zeiss AG, Oberkochen, Germany). After normalization of each iridocyte's spectrum with a specular reflectivity standard (Ocean Optics, STAN-SSH), the maximum reflectivity (R_{max}) and wavelength at peak reflectivity (λ_{max}) were determined (figure 2*a*). Note that the maximum possible value for a perfect reflector is 100%. Care was taken to ensure that the spectra were only from single iridocytes and not confounded by neighbouring iridocytes or algal cells by using a small slit size (0.2 mm) in the spectrometer, corresponding to a region of collection less than 1 µm (compared with iridocyte diameter greater than 5 µm). The depth of field of the objective was 3.8 µm, which was less than the size of the *ca* 10 µm diameter iridocytes.

Such a micro-spectroscopic investigation comes with many other challenges, including the need to ensure collection of normal incidence reflection (given the cone of illumination and collection in a microscope objective), the need to reject reflectivity data from non-normal illumination, and the need to ensure that the slit of the spectrometer is at the image plane to obtain well-isolated spectra from only single iridocytes. These all were accounted for as discussed in detail previously [29,30].

2.2. Transfer matrix analysis

Normalized spectra, obtained as described above, were then fitted using a transfer matrix model [29] to obtain the following parameters of the Bragg stack, with the only assumption being that the low refractive index was that of cytoplasm (=1.35 [31–34]): N, the number of pairs of layers of alternating high and low refractive index; n_H, the refractive index of the high-index layer; and t_L and t_H, the thicknesses of the low- and high-index layers, respectively. A total of 282 spectra were obtained, analysed and fitted from 11 specimens (seven *T. derasa*, one *T. maxima* and three *T. crocea*).

2.3. Finite difference time domain simulations

FDTD simulations were performed using Lumerical's FDTD solutions [35]. We simulated the iridocyte by reducing the model for analysis to a two-dimensional cross section of the iridocyte (as shown schematically in figure 3*a*), with results that can be generalized to three dimensions. The dark blue layers indicate regions of high refractive index, set to the average value $n_{H,Avg} = 1.44$ obtained from our transfer matrix analyses (cf. below); the light blue layers indicate regions of low refractive index, $n_L = 1.35$, based on literature values for cytoplasm as discussed above. The refractive index of the white background, n_{BG}, was set to 1.34 to match that of seawater [36] and thus approximate the slightly lower refractive index of the extracellular environment. The grey region of the perimeter indicates the boundary of the simulation, with boundary conditions set to be absorbing by implementing perfectly matched layers. We simulated excitation of the modelled structure with a plane wave (wavevector along $-y$ indicated by the red arrow in figure 3*a*) for which all source-related fields outside the black box (indicating the boundary of the source region) are set to zero, thereby allowing external monitors (indicated by the dashed blue box) to calculate the shape and strength of fields originating from scattering by structures inside the black box.

All simulations employed an area of $17 \times 17\ \mu m^2$ with greater than or equal to 1 µm space between the outer edge of the structure and the excitation boundary. Excitation was modelled from 300 to 800 nm, with polarization of the excitation field parallel to either the x- or z-direction; results are for the average of values for both polarizations to mimic the effects of the random polarization expected to illuminate the actual iridocytes as the clams are usually found at shallow depths. Post-simulation, the field obtained from the monitor (dashed blue square) was used to calculate the far-field scattering of the structure over the entire wavelength range at 25 discrete frequencies. Based on mesh convergence studies (not shown), the simulation mesh was set to a maximum size of 5 nm. Scattering at each wavelength was normalized to the excitation power at

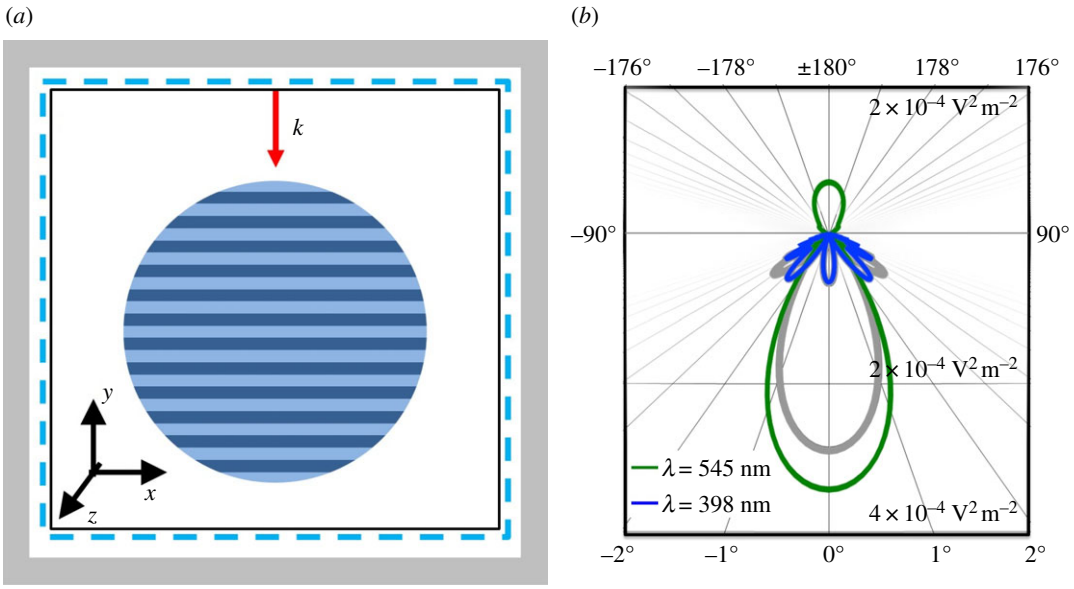

Figure 3. Electromagnetic simulation and light scattering from a sample iridocyte simulation. (*a*) Schematic of the simulation volume in which the circle represents an iridocyte. Light and dark blue regions are regions of low ($n_L = 1.35$) and high refractive index ($n_H = 1.44$), respectively. The red arrow is the wavevector of the incident light and the refractive index of the background (white region) was set to 1.34. (*b*) Stretched polar plot of the simulated far-field (electric field, E^2) scattering by a specific iridocyte; see Results for explanation of the advantage of this format. The origin at the centre represents the position of the iridocyte. Particle diameter = 8 µm; high and low refractive index layer thicknesses, both = 100 nm. The grey trace is provided for reference and shows the scattering at 545 nm of a particle of uniform refractive index = 1.395. Scattering from this uniform particle at 398 nm is identical to that of the structured particle, and underlies the blue trace in the figure.

that wavelength. Fitting of the input excitation to the solar spectrum would introduce only minor variations in the relative intensities of the phenomena we describe and was not done.

To demonstrate the range of reflectance and scattering behaviours that can be achieved by the iridocytes, we varied several parameters over the biologically relevant ranges that we measured experimentally. Diameters were varied from 5 to 15 µm in steps of 1 µm, and thicknesses of the low and high refractive index lamellae were varied from 50 to 150 nm in steps of 10 nm. Given the large range and variation of t_L and t_H seen experimentally, we set the thicknesses of t_L and t_H to be equal to each other as a first approximation.

3. Results

3.1. Micro-spectrophotometry and transfer matrix analyses

Micro-spectrophotometric analyses of the iridocytes allowed us to determine the maximum reflectivity (R_{max}) and its corresponding spectral peak (λ_{max}) from the spectrum obtained from each specimen (figure 2*a*). Peak reflectivity of the sub-cellular Bragg structures varied from 1 to 35%, with comparable variability for each of the three species examined, both for iridocytes within a single specimen and between specimens of the same species. As expected, there was no apparent correlation between R_{max} and λ_{max}. Although the colours reflected from the *T. derasa* and *T. crocea* iridocytes showed clear signs of species-specific clustering, each species contained iridocytes of a wide range of colours.

Analysis of peak reflectivity as a function of wavelength revealed no discernable relationship between the brightness of an iridocyte (R_{max}) and its spectral peak (λ_{max}) (figure 2*a*), with the exception of two cases—a predominantly blue *T. crocea* and a predominantly red *T. derasa* that showed notable bias in the brightness of their blue and red iridocytes, respectively. Overall however, the data do not indicate a systematic bias in any particular colour or species. While most of the specimens exhibited predominance of a few colours, we found iridocytes of all colours in all specimens analysed (cf. figure 1). We thus conclude that the apparent colour of any individual is the result of a bias in its population of iridocytes, rather than differential brightness of iridocytes of any particular colour.

When the fit-derived Bragg-lamellar thicknesses were examined as a function of the wavelengths of the corresponding spectral peaks (λ_{max}), we observed clustering of t_H values in the range 70–140 nm, while t_L values clustered in the range 50–120 nm, with numerous outliers from 50 to 150 nm for both layers (figure 2*b*). The measured average thicknesses are $t_{H,avg} = 84$ nm and $t_{L,avg} = 105$ nm.

Analyses of the fit-derived Bragg-lamellar thicknesses (figure 2*b*) revealed a weak linear relationship between these thicknesses and λ_{max} (Pearson correlation values approximately 0.7 and 0.3 for t_L and t_H, respectively, $p < 0.001$ for both). We note that this weak correlation is not surprising, because λ_{max} depends on the refractive indices of the layers as well as their thicknesses.

Analysis of the measured peak reflectivity (R_{max}) as a function of the fit-derived refractive index (n_H) of the high refractive index region (figure 4) showed a strong linear relationship, with slope progressively increasing with increasing number of pairs of high- and low-index lamellae (all Pearson correlation values more than 0.95, all *p*-values < 0.01). The refractive index of the high-index layer, n_H, was calculated from the data to span a range of 1.39–1.58, with average $n_{H,avg} \pm$ s.d. = 1.44 ± 0.04.

3.2. Finite difference time domain simulations

Figure 3*b* shows a polar plot of the far-field scattering of the electric field intensity (E^2) from a model iridocyte 8 µm in

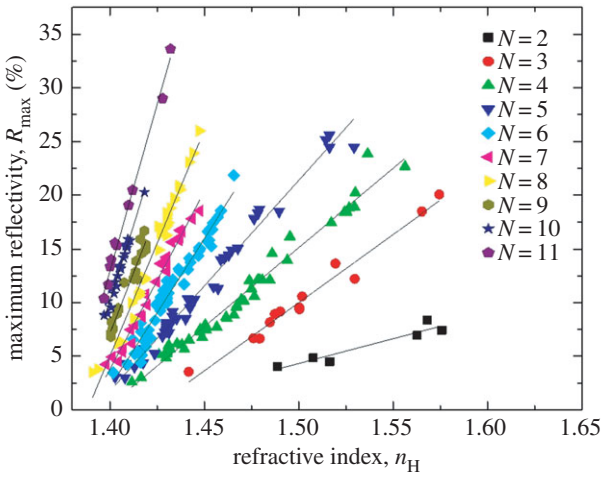

Figure 4. Measured peak reflectivity R_{max} versus the fit-derived refractive index of the high refractive index layer n_H. N = number of pairs of layers in the fitting model with the best fit to the data; black lines are linear fits to the data for individual values of N (Pearson correlation values all more than 0.95, $p < 0.01$).

diameter with 100 nm thick high and low refractive index layers; the origin near the centre, where all the traces converge, indicates the location of the iridocyte. Angles 0° to ±90° correspond to forward scattering and angles ±90° to ±180° correspond to backward scattering ('reflection'). Note that this polar plot is stretched horizontally to show the details of the scattering at small angles, and this necessarily suppresses some of the details at high angles. We specifically chose this stretched presentation to facilitate discernment of important features that had not been recognized or discussed previously. Scattering from the modelled iridocyte is shown for two different wavelengths: 398 nm and 545 nm. The backscattering at 545 nm corresponds closely to the green light reflected by the Bragg stack in the iridocyte; this was verified by calculating the reflection of a Bragg stack of the same dimensions using the transfer matrix method as described above. It is interesting to note that the predominant forward scattering computed also occurs at 545 nm. We further observed that the forward scattering at 398 nm (blue) closely matches the forward scattering (not visible, as the overlap is complete) from a particle of *uniform* refractive index of $(n_H + n_L)/2 = 1.395$ *without* internal Bragg lamellae. For comparison, the grey trace shows the scattering by the same unstructured particle at 545 nm. The relationship and contrast between the scattering from such a particle and from the Bragg-structured iridocyte is most intriguing and will be considered in the Discussion section below.

As discussed below, two further interesting results from the parameter sweep described above are seen in the scattering for two wavelengths, 454 and 627 nm, chosen to approximate the blue and orange colouration (respectively) commonly found in *T. maxima* (figure 5).

4. Discussion

As seen from the results presented here, the relationship between peak reflected colour, wavelength and refractive index is not a simple one. The compound relationship between peak reflectivity (R_{max}) and parameters of the Bragg stack is thus best revealed by the simultaneous correlations with the fit-derived refractive index of the high refractive index layer n_H and the number of pairs of high- and low-index Bragg lamellae (figure 4). The high degree of grouping for a given value of N (Pearson's values for the linear fits indicated by the black lines are all greater than 0.95, $p < 0.01$) suggests simply that the biophysical system analysed does in fact behave as a good Bragg reflector. In addition to the linearity observed within each value of N (which is not required by theory), we see that the slopes of the linear relationships are progressively steeper for higher values of N. This indicates, as would be predicted, that when n_H is high, fewer Bragg lamellae are needed to obtain the same reflectivity. Conversely, for a given value of n_H, reflectivity increases with N.

It is interesting to note that the correlation (as measured by Pearson's R values) between R_{max} and n_H that we measure for various numbers of pairs of Bragg lamellae in giant clam iridocytes (figure 4) is significantly higher than the correlation we previously observed for the tunable iridocytes in squid skin [29]. This difference, indicating the higher quality of fit of the measured spectral data with the predictions of a perfect Bragg reflector for the iridocytes of the giant clam, corresponds to the notably higher structural regularity of the Bragg lamellae in the giant clam (cf. figure 1*d*) relative to the more tortuous lamellae in the squid iridocytes [17,18,26,37]. This result is not unexpected, as the brick-like lamellae in the giant clam iridocytes are fixed and not tunable, and appear to be wholly contained within the cell, in marked contrast with the tunable lamellae of the squid iridocytes that are formed by accordion-like folds or invaginations of the cell's outer membrane [37] and capable of rapid changes in their thickness and spacing triggered by their reflectin-driven dehydration and rehydration [37]. We also note that the refractive index we determined for the high refractive index Bragg lamellae in the live iridocytes of giant clams is specifically determined, in contrast with previous estimates for which that value was either not known precisely [12,22] or overestimated [28] from *in vitro* measurements of dried reflectin (the predominant protein in the reflective Bragg lamellae of squid iridocytes) [38,39].

The FDTD simulations (figures 3 and 5) allow us to develop insights into the optical behaviour of the iridocytes, especially in comparison to similar particles *without* an enclosed Bragg-lamellar structure. Compared with a reference particle of uniform refractive index and identical diameter, the forward scattering (at 0°) by an iridocyte with Bragg lamellae can be *greater* for wavelengths at which the iridocyte is reflective (depending on the size of the particle), as seen in the case illustrated in figure 3*b*. Here, we compare the forward scattering at a wavelength of 545 nm from a particle of uniform refractive index 1.395 (grey trace) to scattering from the iridocyte containing Bragg lamellae (green trace). As expected, these results show that the Bragg stack in the iridocyte back-scatters (reflects) green light, while there is no such reflectance from the unstructured particle with uniform refractive index. Perhaps counterintuitively, however, the iridocyte not only preferentially scatters green light in the forward direction at 0°, but *this forward scattering is greater than that from the diameter-matched particle of identical average but uniform refractive index*. Of course, this does not violate conservation laws as we see that the forward scattering lobes at higher angles (approx. ±3° to ±6°, and even

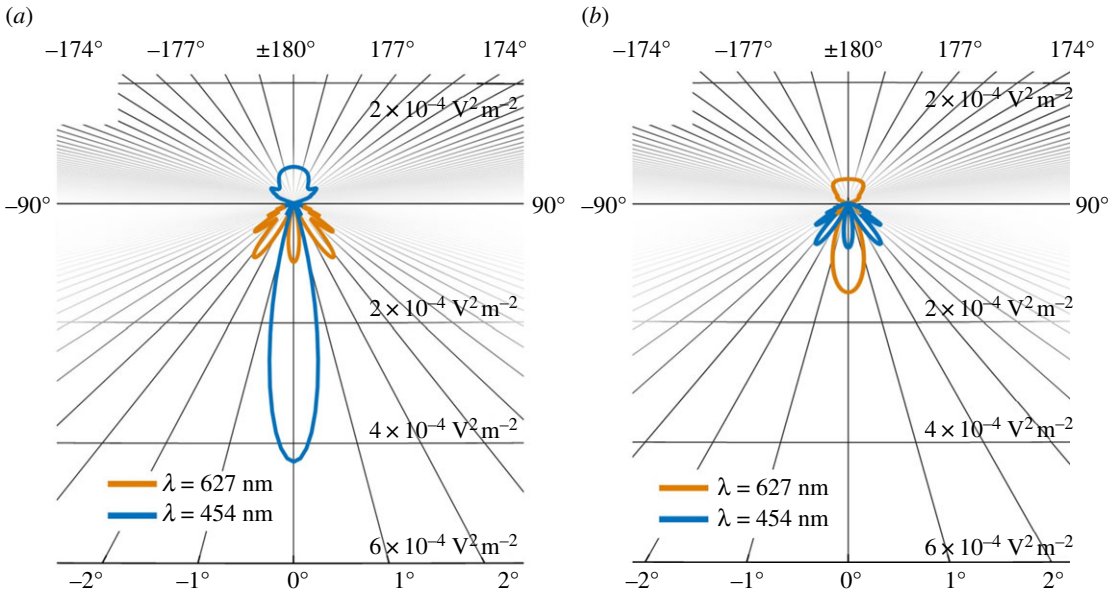

Figure 5. (Stretched) Polar plot of electric field intensity (E^2) scattering of two different iridocytes at 454 nm and 627 nm. The parameters are: (*a*) particle diameter = 12 µm, $t_H = t_L = 80$ nm, (*b*) particle diameter = 9 µm, $t_H = t_L = 110$ nm.

higher angles, though not discernable in this figure) are suppressed. It is for the same reason that the scattered energy at 545 nm looks higher than that at 398 nm; the scattering profile at 398 nm has many small scattering lobes at higher angles (from $\pm 6^\circ$ to $\pm 90^\circ$) that are absent from the scattering profile at 545 nm. We attribute this suppression of higher angle scattering lobes to the phase relationship imposed by the Bragg stack that promotes reflection (and allows some transmission) at the design wavelength, *and* suppresses scattering at higher angles—thus forcing the scattering to be primarily either in the directly forward (0°) or backward directions. Interestingly, our simulations indicate that at wavelengths far from the wavelength of Bragg reflection (e.g. 398 nm), the scattering by an iridocyte of a given diameter is identical to that from a particle of the same average, but uniform, refractive index without lamellae.

Test simulations in which the Bragg stacks were not normal to the direction of the illumination showed two things: (i) the angle of reflection at the appropriate Bragg wavelength simply followed the law of reflection and (ii) the scattering in the forward direction was in the same direction as the incident light, which is easily understood by considering the following. Without the Bragg structure, the iridocyte would behave as an angularly agnostic, Mie-scattering sphere; the Bragg structure simply acts as a slab of higher index medium with parallel faces, causing forward scattering in the same direction as the incident light. Thus, only normal incidence simulations are presented here.

Two specific cases (figure 5) illustrate behaviours of the iridocytes that provide insight into their unique optical properties and their possible function in giant clams. As we will see below, despite the rough approximation of setting $t_L = t_H$, the preferential forward scattering by a Bragg-structured iridocyte is maintained. Considering the modelled iridocyte that reflects 454 nm (blue) but not 627 nm, we see in figure 5*a* that even though an iridocyte back-reflects blue light, the directly forward-scattered light (0°) is *also* predominantly blue and not orange, while the light scattered forward at higher angles is orange. Similarly, in figure 5*b*, the back-reflected *and* directly forward-scattered light at 0° is orange, and the light forward scattered at higher angles is blue. Thus, by carefully tuning their shape, size and optical parameters, we can design model iridocytes for which the predominantly forward-scattered light is the same colour as the predominantly reflected light, while suppressing forward scattering at other wavelengths.

While the variation of scattering angles produced by variation in the chosen parameters is small—whether for the real iridocytes in the giant clam or any potential synthetic system—the final effect in the animal will depend on the cumulative effect from multiple scattering events, especially at wavelengths for which the scattering angle is relatively large (e.g. 398 nm in figure 3*b*, 627 nm in figure 5*a* and 454 nm in figure 5*b*). In the mantle of the giant clam, the iridocytes are distributed in a layer over 20 iridocytes deep [28], multiplicatively increasing the total divergence of scattering from each iridocyte (*ca* $\pm 6^\circ$) to potentially yield a collective scattering cone as large as $\pm 90^\circ$. Such a large collective scattering angle will produce very different optical environments at different depths within the clam tissue. For example, in the case of the blue reflective iridocyte, our simulations discussed above indicate that at shallow depths into the tissue, wavelengths other than blue are scattered yielding a broadband diffuse light environment, while at greater depths into the tissue the blue light that is preferentially scattered forward will result in downwelling illumination that is more blue. Similarly, for a primarily orange-reflecting giant clam, at shallow depths into the tissue the light is primarily diffuse and broadband (though somewhat deficient in the orange wavelength range), while at greater depths into the tissue the light is primarily downwelling and more orange.

While we can expect the above-described light environments within giant clams that reflect a specific colour, we can expect something different from those giant clams that appear white as a result of the reflectance from a collection of differently coloured iridocytes [40]. Based on the above understanding, we expect that the internal light environment throughout the tissue would be broadband.

5. Summary and conclusion

The quantitative experimental measurements and electromagnetic (FDTD) simulations of Bragg-structured clam iridocytes considered herein predict that for all values of iridocyte size and wavelength investigated, more than 90% of incident solar energy is carried by photons that are forward scattered into the clam tissue in a wavelength-specific manner. It also was seen that enhanced forward scattering can occur at specific wavelengths from internally Bragg-structured versus unstructured iridocytes. This enhancement of downwelling scattering comes at the expense of scattering at higher angles that is otherwise seen from unstructured iridocytes. The iridescence of the clam mantle is largely due to back reflection at these same wavelengths; i.e. the preferential downwelling light from forward scattering is similar in colour to mantle iridescence. Formally, these FDTD solutions reveal the wavelength- and angle-specific distributions of electromagnetic field strength that result in part from the spatially differentiated phase delay uniquely imparted by the interaction of light (waves) with the Bragg lamellae in the Mie-scattering structures.

These results and further insight complement and extend the spectrophotometric measurements in the clam and simulations by a different method of Holt *et al.* [28], who showed that forward Mie scattering, coupled with variations in iridocyte orientation and diurnal sun angle, can uniformly illuminate the vertical columns of photosynthetically active microalgae that live endosymbiotically in the clams' gastric diverticula [13,41]. We have systematically measured and modelled multiple iridocyte parameters and discovered that at certain values the reflected colour can match the wavelength of the predominantly forward-scattered photons. Additionally, the results we report offer potentially significant new insights for our growing understanding of the photophysics of the iridocytes, and the physiological, ecological and evolutionary complexities of the symbiotic relationship between giant clams and the *Symbiodinium* species complex of endosymbiotic microalgae [10,15,41–45].

Our results further suggest that variation of the internal photic environment in the animal host, as a consequence of variations in the ultrastructure of their iridocytes, might establish optimal habitats for different clades of algae that preferentially use different parts of the solar spectrum for photosynthesis. If this should prove to be the case, reflection of a particular colour from the mantle iridocytes might provide a convenient diagnostic for recognition of the light environment within a giant clam, and consequently, for the subtype of alga it might harbour and rely upon. In genetic terms, this hypothesis posits that the observed colour polymorphism of the giant clams may be correlated with a polymorphism in photosynthetic action spectrum of the endosymbiotic *Symbiodinia*, and specifically, that the action spectrum of the predominant algal clade in each colour morph may be optimized to match the forward-scattered (and back-reflected) photic environment in the host clam. If true, this might be an important consideration for maintenance of genetic diversity of the tridacnids, both as a buffer of environmental or climate change, and as intensive aquaculture cultivation, harvesting and international piracy of these species for food, shell and the aquarium trade are markedly on the rise.

Mie-scattering iridocytes similar to those in the giant clam can be seen to have evolved earlier in molluscan phylogeny, albeit adapted for different functionality. For example, cells similar in dimension and structure, with highly regular internal Bragg lamellae orthogonal to the incident light, act as colour filters in front of the source of bioluminescence in photophores of the mesopelagic squid *Abralia trigonura* [46]. The photophysics of these cells appears quite similar to that we have modelled and analysed here, yielding blue light by Bragg-modulated (thin-film interference-modulated) Mie scattering. In the giant clam, these cells direct wavelength-specific solar photons forward and deep into the tissue, while in the luminescent photophore, the comparable wavelength-specific forward scattering directs photons outward.

The simulation results presented here indicate that both the spectral and angular scattering behaviour of an iridocyte depend on, and can be exquisitely controlled by the diameter of the cell, the thicknesses of the high and low refractive index Bragg lamellae and the refractive indices of those lamellae. Consequently, the unique scattering displayed by structures modelled on the giant clam iridocytes could be used to control the photic environment in solar cells to increase their efficiency. A case in point is the tandem solar cell, in which different photoactive layers absorb light of progressively longer wavelengths. With absorption of blue light in the top layer and red in a lower layer, for example, improvement could be attained by addition of a layer of iridocyte-like particles that scatter blue light at higher angles while preferentially scattering red light forward. This would simultaneously increase the path-length of blue light in the top absorbing layer while efficiently transmitting red light to the lower, red-absorbing layer.

Data accessibility. The data relating to this study are contained in the electronic supplementary material.

Competing interests. The authors have no competing interests.

Funding. This research was supported by a grant from the Army Research Office (no. W911NF-10-1-0139) and by the Institute for Collaborative Biotechnologies through grant no. W911NF-09-0001 from the US Army Research Office.

Acknowledgements. The content does not necessarily reflect the position or policy of the Government, and no official endorsement should be inferred. We thank Mary Baum for figure 1*a*.

References

1. Copland JW, Lucas JS. 1988 *Giant clams in Asia and the Pacific*. Canberra, Australia: Australian Centre for International Agricultural Research.
2. Thomas WH. 1970 On nitrogen deficiency in tropical Pacific oceanic phytoplankton: photosynthetic parameters in poor and rich water. *Limnol. Oceanogr.* **15**, 380–385. (doi:10.4319/lo.1970.15.3.0380)
3. Dufour P, Charpy L, Bonnet S, Garcia N. 1999 Phytoplankton nutrient control in the oligotrophic South Pacific subtropical gyre (Tuamotu Archipelago). *Mar. Ecol. Prog. Ser.* **179**, 285–290. (doi:10.3354/meps179285)
4. Toonen RJ, Nakayama T, Ogawa T, Rossiter A, Delbeek JC. 2012 Growth of cultured giant clams (*Tridacna* spp.) in low pH, high-nutrient seawater: species-specific effects of substrate and supplemental feeding under acidification. *J. Mar. Biol. Assoc. UK* **92**, 731–740. (doi:10.1017/S0025315411000762)
5. Knop D. 1996 *Giant clams: a comprehensive guide to the identification and care of tridacnid clams*,

illustrated edition. Ettlingen, Germany: Two Little Fishies Inc.

6. Klumpp DD *et al.* 1994 Nutritional ecology of the giant clams, *Tridacna tevoroa* and *T. derasa* from Tonga: influence of light on filter-feeding and photosynthesis. *Mar. Ecol. Prog. Ser.* **107**, 147–156. (doi:10.3354/meps107147)
7. Carlos AA, Baillie BK, Kawachi M, Maruyama T. 1999 Phylogenetic position of *Symbiodinium* (dinophyceae) isolates from tridacnids (bivalvia), cardiids (bivalvia), a sponge (porifera), a soft coral (anthozoa), and a free-living strain. *J. Phycol.* **35**, 1054–1062. (doi:10.1046/j.1529-8817.1999.3551054.x)
8. Hean RL, Cacho OJ. 2003 A growth model for giant clams *Tridacna crocea* and *T. derasa*. *Ecol. Model.* **163**, 87–100. (doi:10.1016/S0304-3800(02)00400-3)
9. Ishikura M, Hagiwara K, Takishita K, Haga M, Iwai K, Maruyama T. 2004 Isolation of new *Symbiodinium* strains from tridacnid giant clam (*Tridacna crocea*) and sea slug (*Pteraeolidia ianthina*) using culture medium containing giant clam tissue homogenate. *Mar. Biotechnol.* **6**, 378–385. (doi:10.1007/s10126-004-1800-7)
10. DeBoer TS, Baker AC, Erdmann MV. 2011 Patterns of *Symbiodinium* distribution in three giant clam species across the biodiverse Bird's Head region of Indonesia. *Mar. Ecol. Prog. Ser.* **444**, 117–132. (doi:10.3354/meps09413)
11. Vermeij GJ. 2013 The evolution of molluscan photosymbioses: a critical appraisal. *Biol. J. Linn. Soc.* **109**, 497–511. (doi:10.1111/bij.12095)
12. Norton JH, Jones GW. 1992 *The giant clam: an anatomical and histological atlas*. Canberra, Australia: Australian Centre for International Agricultural Research.
13. Yellowlees D, Dionisio-Sese ML, Masuda K, Maruyama T, Abe T, Baillie B, Tsuzuki M, Miyachi S. 1993 Role of carbonic anhydrase in the supply of inorganic carbon to the giant clam—zooxanthellate symbiosis. *Mar. Biol.* **115**, 605–611. (doi:10.1007/BF00349368)
14. Lucas JS. 1994 The biology, exploitation, and mariculture of giant clams (Tridacnidae). *Rev. Fish. Sci.* **2**, 181–223. (doi:10.1080/10641269409388557)
15. Klumpp DW, Griffiths CL. 1994 Contributions of phototrophic and heterotrophic nutrition to the metabolic and growth requirements of four species of giant clam (Tridacnidae). *Mar. Ecol. Prog. Ser.* **115**, 103–115. (doi:10.3354/meps115103)
16. Leggat W, Marendy EM, Baillie B, Whitney SM, Ludwig M, Badger MR, Yellowlees D. 2002 Dinoflagellate symbioses: strategies and adaptations for the acquisition and fixation of inorganic carbon. *Funct. Plant Biol.* **29**, 309–322. (doi:10.1071/PP01202)
17. Mirow S. 1971 Skin color in the squids *Loligo pealii* and *Loligo opalescens*. II. Iridophores. *Z. Zellforsch. Mikrosk. Anat.* **125**, 176–190. (doi:10.1007/BF00306787)
18. Cooper K, Hanlon R. 1986 Correlation of iridescence with changes in iridophore platelet ultrastructure in the squid *Lolliguncula brevis*. *J. Exp. Biol.* **121**, 451–455.
19. Cooper KM, Hanlon RT, Budelmann BU. 1990 Physiological color change in squid iridophores. *Cell Tissue Res.* **259**, 15–24. (doi:10.1007/BF00571425)
20. Mäthger L, Hanlon R. 2007 Malleable skin coloration in cephalopods: selective reflectance, transmission and absorbance of light by chromatophores and iridophores. *Cell Tissue Res.* **329**, 179–186. (doi:10.1007/s00441-007-0384-8)
21. Sutherland RL, Mathger LM, Hanlon RT, Urbas AM, Stone MO. 2008 Cephalopod coloration model. I. Squid chromatophores and iridophores. *J. Opt. Soc. Am. A* **25**, 588–599. (doi:10.1364/JOSAA.25.000588)
22. Kawaguti S. 1966 Electron microscopy on the mantle of the giant clam with special references to zooxanthellae and iridophores. *Biol. J. Okayama Univ.* **12**, 81–92.
23. Kamishima Y. 1990 Organization and development of reflecting platelets in iridophores of the giant clam, *Tridacna crocea* Lamarck: developmental biology. *Zool. Sci.* **7**, 63–72.
24. Griffiths D, Winsor H, Luongvan T. 1992 Iridophores in the mantle of giant clams. *Aust. J. Zool.* **40**, 319–326. (doi:10.1071/ZO9920319)
25. Brocco SL. 1976 The ultrastructure of the epidermis, dermis, iridophores, leucophores, and chromatophores of *Octopus dofleini* Martini (Cephalopoda: Octopoda). PhD thesis, University of Washington, Seattle, WA, USA.
26. Cloney RA, Brocco SL. 1983 Chromatophore organs, reflector cells, iridocytes and leucophores in cephalopods. *Am. Zool.* **23**, 581–592. (doi:10.1093/icb/23.3.581)
27. Yonge CM. 1975 Giant clams. *Sci. Am.* **232**, 96–105. (doi:10.1038/scientificamerican0475-96)
28. Holt AL, Vahidinia S, Gagnon YL, Morse DE, Sweeney AM. 2014 Photosymbiotic giant clams are transformers of solar flux. *J. R. Soc. Interface* **11**, 20140678. (doi:10.1098/rsif.2014.0678)
29. Ghoshal A, DeMartini DG, Eck E, Morse DE. 2013 Optical parameters of the tunable Bragg reflectors in squid. *J. R. Soc. Interface* **10**, 20130386. (doi:10.1098/rsif.2013.0386)
30. Ghoshal A, DeMartini DG, Eck E, Morse DE. 2014 Experimental determination of refractive index of condensed reflectin in squid iridocytes. *J. R. Soc. Interface* **11**, 20140106. (doi:10.1098/rsif.2014.0106)
31. Bereiter-Hahn J, Fox CH, Thorell B. 1979 Quantitative reflection contrast microscopy of living cells. *J. Cell Biol.* **82**, 767–779. (doi:10.1083/jcb.82.3.767)
32. Dunn AK. 1997 Light scattering properties of cells. Thesis, University of Texas at Austin, Austin, TX.
33. Curl CL *et al.* 2005 Refractive index measurement in viable cells using quantitative phase-amplitude microscopy and confocal microscopy. *Cytometry A* **65A**, 88–92. (doi:10.1002/cyto.a.20134)
34. Jin YL, Chen JY, Xu L, Wang PN. 2006 Refractive index measurement for biomaterial samples by total internal reflection. *Phys. Med. Biol.* **51**, N371. (doi:10.1088/0031-9155/51/20/N02)
35. FDTD Solutions. Lumerical Solutions, Inc. www.lumerical.com.
36. Austin RW, Halikas G. 1976 *The index of refraction of seawater*. Technical report. La Jolla, CA: Scripps Institution of Oceanography.
37. DeMartini DG, Krogstad DV, Morse DE. 2013 Membrane invaginations facilitate reversible water flux driving tunable iridescence in a dynamic biophotonic system. *Proc. Natl Acad. Sci. USA* **110**, 2552–2556. (doi:10.1073/pnas.1217260110)
38. Denton EJ, Land MF. 1971 Mechanism of reflexion in silvery layers of fish and cephalopods. *Proc. R. Soc. Lond. B* **178**, 43–61. (doi:10.1098/rspb.1971.0051)
39. Kramer RM, Crookes-Goodson WJ, Naik RR. 2007 The self-organizing properties of squid reflectin protein. *Nat. Mater.* **6**, 533–538. (doi:10.1038/nmat1930)
40. Ghoshal A, Eck E, Morse DE. 2016 Biological analogs of RGB pixelation yield white coloration in giant clams. *Optica* **3**, 108–111. (doi:10.1364/OPTICA.3.000108)
41. Hennige SJ, Suggett DJ, Warner ME, McDougall KE, Smith DJ. 2008 Photobiology of *Symbiodinium* revisited: bio-physical and bio-optical signatures. *Coral Reefs* **28**, 179–195. (doi:10.1007/s00338-008-0444-x)
42. Hirose E, Iwai K, Maruyama T. 2006 Establishment of the photosymbiosis in the early ontogeny of three giant clams. *Mar. Biol.* **148**, 551–558. (doi:10.1007/s00227-005-0119-x)
43. Belda-Baillie CA, Sison M, Silvestre V, Villamor K, Monje V, Gomez ED, Baillie BK. 1999 Evidence for changing symbiotic algae in juvenile tridacnids. *J. Exp. Mar. Biol. Ecol.* **241**, 207–221. (doi:10.1016/S0022-0981(99)00079-9)
44. Knowlton N, Rohwer F. 2003 Multispecies microbial mutualisms on coral reefs: the host as a habitat. *Am. Nat.* **162**, S51–S62. (doi:10.1086/378684)
45. LaJeunesse TC, Wham DC, Pettay DT, Parkinson JE, Keshavmurthy S, Chen CA. 2014 Ecologically differentiated stress-tolerant endosymbionts in the dinoflagellate genus *Symbiodinium* (Dinophyceae) Clade D are different species. *Phycologia* **53**, 305–319. (doi:10.2216/13-186.1)
46. Young RE, Arnold JM. 1982 The functional-morphology of a ventral photophore from the mesopelagic squid, *Abralia trigonura*. *Malacologia* **23**, 135–163.